

Towards monitoring localized CO₂ emissions from space: co-located regional CO₂ and NO₂ enhancements observed by the OCO-2 and S5P satellites

Maximilian Reuter¹, Michael Buchwitz¹, Oliver Schneising¹, Sven Krautwurst¹, Christopher W. O'Dell², Andreas Richter¹, Heinrich Bovensmann¹, and John P. Burrows¹

¹Institute of Environmental Physics, University of Bremen, Germany

²Colorado State University, Fort Collins, CO, USA

Correspondence: Maximilian Reuter (mail@maxreuter.org)

Abstract. Despite its key role for climate change, large uncertainties persist in our knowledge of the anthropogenic emissions of carbon dioxide (CO₂) and no global observing system exists allowing to monitor emissions from localized CO₂ sources with sufficient accuracy. The Orbiting Carbon Observatory-2 (OCO-2) satellite allows retrievals of the column-average dry-air mole fractions of CO₂ (XCO₂). However, regional column-average enhancements of individual point sources are usually small

5 compared to the background concentration and its natural variability and often not much larger than the satellite's measurement noise. This makes the unambiguous identification and quantification of anthropogenic emission plume signals challenging. NO₂ is co-emitted with CO₂ when fossil fuels are combusted at high temperatures. It has a short lifetime of the order of hours so that NO₂ columns often greatly exceed background and noise levels of modern satellite sensors near sources which makes it a suitable tracer of recently emitted CO₂. Based on six case studies (Moscow, Russia; Lipetsk, Russia; Baghdad, Iraq; 10 Medupi and Matimba power plants, South Africa; Australian wildfires; and Nanjing, China), we demonstrate the usefulness of simultaneous satellite observations of NO₂ and XCO₂. For this purpose, we analyze co-located regional enhancements of XCO₂ observed by OCO-2 and NO₂ from the Sentinel-5 Precursor (S5P) satellite and estimate the CO₂ plume's cross-sectional fluxes. We take advantage of the nearly simultaneous NO₂ measurements with S5P's wide swath and small measurement noise by identifying the source of the observed XCO₂ enhancements, excluding interference with remote upwind sources, allowing 15 to adjust the wind direction, and by constraining the shape of the CO₂ plumes. We compare the inferred cross-sectional fluxes with the Emissions Database for Global Atmospheric Research (EDGAR), the Open-Data Inventory for Anthropogenic Carbon dioxide (ODIAC), and, in the case of the Australian wildfires, with the Global Fire Emissions Database (GFED). The inferred cross-sectional fluxes range from 31 MtCO₂/a to 153 MtCO₂/a with uncertainties (1σ) between 23% and 72%. For the majority of analyzed emission sources, the estimated cross-sectional fluxes agree within their uncertainty with either 20 EDGAR or ODIAC or lie in between them. We assess the contribution of multiple sources of uncertainty and find that the dominating contributions are related to the computation of the effective wind speed normal to the plume's cross-section. The flux uncertainties are expected to be reduced by the planned European Copernicus anthropogenic CO₂ monitoring mission (CO2M) which will not only provide precise measurements with high spatial resolution but also imaging capabilities with a

wider swath of simultaneous XCO₂ and NO₂ observations. Such a mission, in particular as a constellation of satellites, will deliver CO₂ emission estimates from localized sources at an unprecedented frequency and level of accuracy.

1 Introduction

Carbon dioxide (CO₂) is the most important anthropogenic greenhouse gas and driver for climate change. By September 5 2018, 195 member states of the UNFCCC (United Nations Framework Convention on Climate Change) have signed the Paris agreement with the long-term goal to keep the increase in global average temperatures relative to pre-industrial levels well below 2°C. Actions need to be taken to halve anthropogenic greenhouse gas emissions (including CO₂) each decade after reaching peak emissions in 2020 (Rockström et al., 2017). However, there are still large uncertainties in the anthropogenic emissions and no global observing system exists allowing to monitor country emissions and their changes with sufficient 10 accuracy (e.g., Ciais et al., 2014; Pinty et al., 2017).

CO₂ is long-lived and well-mixed in the atmosphere and its largest gross fluxes are of natural origin (photosynthesis and respiration). As a result, regional column-average enhancements of individual anthropogenic point sources are usually small compared with the background concentration and its natural variability and often not much larger than the satellite's measurement noise (Bovensmann et al., 2010). This makes the identification of anthropogenic plume signals with past (SCIAMACHY 15 (SCanning Imaging Absorption SpectroMeter for Atmospheric CHartographY, Burrows et al., 1995; Bovensmann et al., 1999)) and current (GOSAT (Greenhouse Gases Observing Satellite, Kuze et al., 2009), OCO-2 (Orbiting Carbon Observatory-2, Crisp et al., 2004)) satellite sensors difficult and the quantification of anthropogenic emissions a challenging task. Usually, the latter requires knowledge of the source position and assumptions on plume formation (e.g., Nassar et al., 2017; Heymann et al., 2017) or statistical approaches applied on larger areas and/or time periods (e.g., Schneising et al., 2013; Buchwitz et al., 2017).

20 Reuter et al. (2014) followed an alternative approach to identify anthropogenic regional CO₂ enhancements by analyzing simultaneous satellite observations of tropospheric nitrogen dioxide (NO₂) vertical columns and column-average dry-air mole fractions of CO₂ (XCO₂). Nitrogen monoxide (NO) is formed and emitted to the atmosphere when fossil fuels are combusted at high temperatures. In the atmosphere, it reacts rapidly with ozone (O₃) and at a much slower rate via a termolecular reaction with oxygen (O₂) to form NO₂. The tropospheric daytime concentrations of NO₂ are coupled with the concentrations of NO 25 and O₃ by the Leighton photo-stationary state. NO₂ has a short lifetime of the order of hours so that its vertical column densities often greatly exceed background and noise levels of modern satellite sensors near sources (Richter et al., 2005) making it a suitable tracer of recently emitted CO₂.

In contrast to SCIAMACHY used by Reuter et al. (2014), OCO-2 has no NO₂ sensor aboard. However, with the launch of the S5P satellite (Sentinel-5 Precursor, Veefkind et al., 2012) in October 2017, NO₂ observations with unprecedented spatial 30 resolution and global daily coverage became available. Here we use this data to identify OCO-2 XCO₂ enhancements which can be attributed to localized (up to city-scale) emissions for which we estimate the plume's cross-sectional CO₂ fluxes.

In the next section, we describe the used OCO-2 XCO₂ and S5P NO₂ data sets and the developed co-location method. In section 2, we describe the used plume detection and scenario selection method as well as the cross-sectional flux estimation method. The results of our case study analyses are presented and discussed in section 3 and 4, respectively.

2 Data sets and methods

5 2.1 XCO₂

The Orbiting Carbon Observatory-2 (OCO-2, Crisp et al., 2004) was launched in 2014 aiming at continuing and improving XCO₂ observations from space. OCO-2 is part of the A-train satellite constellation and flies in a sun-synchronous orbit whose ascending node crosses the equator on 13:36 local time. It measures the solar backscattered radiance in three independent wavelength bands in the spectral regions of the near infrared (NIR) and short wave infrared (SWIR): the O₂-A band at 10 around 760 nm, the weak CO₂ band at around 1610 nm, and the strong CO₂ band at around 2060 nm. OCO-2 is operated in a near-push-broom fashion and has eight parallelogram-shaped footprints across track with a spatial resolution at ground of $\leq 1.29 \text{ km} \times 2.25 \text{ km}$.

We use NASA's operational bias corrected OCO-2 L2 Lite XCO₂ product v9 (Kiel et al., 2019, see Fig. 1a for an example) which we obtained from <https://daac.gsfc.nasa.gov>. The product is rigorously pre- and post-filtered for potentially unreliable 15 soundings including, e.g., cloud and aerosol contaminated scenes. Additionally, the OCO-2 retrieval algorithm accounts for light scattering at optically thin aerosol layers by fitting the optical depth and height of two lower-atmosphere aerosol layers and the optical depth of a stratospheric aerosol layer (O'Dell et al., 2018). The OCO-2 v9 data set has an improved bias correction approach that results in reduced biases particularly over areas of rough topography.

The OCO-2 XCO₂ product includes an uncertainty estimate which we use for our study. For the selected scenarios, the 20 reported single sounding uncertainty lies typically in the range of 0.4 ppm to 0.7 ppm which is similar to estimates based on the standard deviation of the difference of succeeding soundings. The validation study of Reuter et al. (2017) estimated that the single sounding precision relative to ground based Total Carbon Column Observing Network (TCCON) data is about 1.3 ppm. However, this includes, e.g., the noise of the validation data set and a larger pseudo-noise component due to spatial 25 and temporal representation errors when co-locating OCO-2 with the validation data and it shall be noted that the study of Reuter et al. (2017) analyzed a predecessor NASA OCO-2 XCO₂ data set (v7 instead of v9).

2.2 NO₂

The TROPOspheric Monitoring Instrument (TROPOMI) on Sentinel-5 Precursor was launched in October 2017 into a sun-synchronous orbit with an ascending node local equator crossing time of 13:30 (Veefkind et al., 2012). TROPOMI is a nadir viewing imaging grating spectrometer for the UV/visible spectral region with additional channels in the NIR and SWIR, extending 30 the existing data records of the GOME (Global Ozone Monitoring Experiment), SCIAMACHY, OMI (Ozone Monitoring Instrument), and the GOME-2 missions. It has a swath width of about 2600 km and in comparison to previous instruments a

much better spatial resolution of $3.5\text{ km} \times 7\text{ km}$ at nadir at similar signal to noise ratio per measurement. Here we use radiances in the spectral region 425 nm–465 nm to retrieve NO_2 slant columns with a standard Differential Optical Absorption Spectroscopy (DOAS) retrieval developed for previous satellite instruments (Richter et al., 2011), followed by a de-striping step as described by Boersma et al. (2007). Slant columns are defined as the absorber concentration integrated along the light path, 5 and thus depend on both, the atmospheric NO_2 profile, and the light path of the individual measurement.

The random noise of our S5P slant columns has been estimated from the scatter of observations over a clean Pacific region (10°S–10°N, 160°E–230°E). In order to account for the viewing angle dependency of the slant columns, a geometric air mass factor has been computed using only the instrument's viewing zenith angle. The evaluation suggests that the random noise (1σ) of our S5P slant column product is typically $5 \cdot 10^{14} \text{ molec./cm}^2$, while enhancements near sources often exceed 10 $10^{16} \text{ molec./cm}^2$. For individual soundings, the uncertainty can differ depending on viewing geometry and surface reflectance.

In order to extract the tropospheric vertical columns, usually, first the stratospheric contribution to the retrieved slant columns needs to be removed and then the light path dependency of the remaining tropospheric slant columns is corrected for by dividing through a scene dependent air mass factor. In this study, another approach is taken as only localized enhancements are evaluated. By subtracting the surrounding background values (section 2.5), both the stratospheric contribution and any 15 tropospheric background are removed from the signal as they are both smooth on scales of a few tens of kilometers discussed here. What remains is the slant column plume signal of the lower troposphere from which we derive information on the CO_2 plume.

2.3 Co-location of OCO-2 and S5P data

OCO-2 and S5P fly both in sun-synchronous orbits with similar equator crossing times of their ascending nodes and orbit 20 times of about 100 minutes. S5P has a swath width of about 2600 km which provides nearly global coverage each day. For these reasons, basically each scene observed by OCO-2 is also observed by S5P within a maximum time difference of about 50 minutes. We project the S5P and OCO-2 data of the same day in a surrounding of a potential target on a high resolution ($0.001^\circ \times 0.001^\circ$) grid to compute NO_2 averages representative for the footprints of the CO_2 soundings (see Fig. 1c for an example).

25 2.4 Geophysical data bases

As input for the computation of the cross-sectional fluxes (section 2.5), we compute the number of dry air particles in the atmospheric column from meteorological profiles which we read at the same time with the wind information from the ECMWF (European Centre for Medium range Weather Forecast) ERA5 (fifth generation of ECMWF atmospheric reanalyzes) data archive at $0.25^\circ \times 0.25^\circ \times$ hourly resolution. This data archive provides also an uncertainty estimate of the wind information 30 from an ensemble statistic but at a reduced resolution of about $0.5^\circ \times 0.5^\circ \times$ three hours.

We compare the inferred cross-sectional CO_2 fluxes with the following emission data bases. The Emissions Database for Global Atmospheric Research (EDGAR v4.3.2, <https://edgar.jrc.ec.europa.eu>) provides information on anthropogenic CO_2 emissions at $0.1^\circ \times 0.1^\circ \times$ annually resolution. EDGAR v4.3.2 ends in 2012 and we use the data of that year for our comparisons.

The Open-Data Inventory for Anthropogenic Carbon dioxide (ODIAC v2017, <http://db.cger.nies.go.jp/dataset/ODIAC>, Oda et al., 2018) provides also information on annual anthropogenic CO₂ emissions but at a finer resolution (1 km × 1 km × monthly) and the data base ends in 2016. For the reason of comparability, we re-gridded the ODIAC emissions to the EDGAR resolution (0.1° × 0.1° × annual) and use 2012 data as baseline. Additionally, we use ODIAC v2017 data re-gridded to 0.1° × 0.1° × monthly resolution. The Global Fire Emissions Database (GFED v4.1s, <https://www.globalfiredata.org>) provides information on CO₂ emissions from wildfires at a resolution of 0.25° × 0.25° × 3 hours which we re-gridded to 0.1° × 0.1° resolution for a six hours average ending approximately at the time of the overpass.

2.5 Flux estimation

S5P's spatial resolution is considerably coarser than that of OCO-2. Consequently for our case studies, we concentrate on plumes which are significantly larger than the swath width of OCO-2. This means that for the selected scenarios, OCO-2 sees actually only a cross-section of a plume (see Fig. 1c for an example).

We model the cross-sectional NO₂ columns along the OCO-2 orbit by a linear polynomial, accounting for large scale variations of the background values, overlayed by a Gaussian function describing the enhancement within the plume. Simultaneously, the cross-sectional CO₂ concentrations are modeled in a similar manner. However, the width of the CO₂ Gaussian function is constrained to equal the width of the NO₂ Gaussian function. This means, the plume shape is determined from the NO₂ measurements, but we allow for a shifted position of the maximum in order to account for potential plume displacements resulting from different overpass times. Additionally, it shall be noted that the CO₂ and NO₂ plumes may have small differences, e.g., due to different decay rates of NO₂ in different altitudes. These differences, however, are considered minor compared with the precision of the XCO₂ soundings. Specifically, the co-located NO₂ and XCO₂ values along the distance in OCO-2's flight direction x are fitted with the maximum likelihood method by the following vector function:

$$\begin{pmatrix} \text{NO}_2 \\ \text{XCO}_2 \end{pmatrix} = \begin{pmatrix} a_0 + a_1 x + a_2 e^{-4 \ln(2) (x-a_3)^2 a_4^{-2}} \\ a_5 + a_6 x + a_7 e^{-4 \ln(2) (x-a_8)^2 a_4^{-2}} \end{pmatrix} \quad (1)$$

The free fit parameters a_{0-8} correspond to the polynomial coefficients of the background values ($a_{0,1,5,6}$), the amplitudes ($a_{2,7}$), shifts ($a_{3,8}$), and the full width at half maximum (FWHM, a_4) of the Gaussian functions. We force the FWHM to be constrained entirely by the NO₂ measurements by setting the CO₂ part of the corresponding Jacobian artificially to zero. However, we expect only little differences to a combined FWHM fit because of the lower relative noise of the NO₂ measurements.

Integration over the Gaussian enhancement results in the cross-sectional CO₂ flux F_{CO_2} (mass of CO₂ per time) of the plume depending on the FWHM a_4 , the amplitude of the XCO₂ enhancement a_7 , the effective wind speed v_e within the plume normal to the OCO-2 orbit, and the number of dry air particles in the atmospheric column n_e :

$$F_{\text{CO}_2} = \frac{1}{2} \sqrt{\frac{\pi}{\ln(2)}} \frac{M_{\text{CO}_2}}{N_A} n_e a_4 a_7 v_e \quad (2)$$

5

Here, M_{CO_2} is the molar mass of CO₂ (44.01 g/mol) and N_A the Avogadro constant ($6.02214076 \cdot 10^{23} \text{ mol}^{-1}$). We approximate the number of dry air particles n_e and the effective wind speed's normal v_e from ECMWF ERA5 meteorological profiles at the position of the maximum of the fitted Gaussian XCO₂ function. In regions with large variations of the surface elevation 10 or wind conditions within the plume's cross-section, it might be appropriate to account for variations in the number of dry air particles and/or the wind conditions when integrating over the Gaussian enhancement.

We manually adjust the ECMWF wind direction (not the wind speed) to subjectively fit the plume direction observed in the NO₂ fields (e.g., Fig. 1a). The manual adjustment to wind direction but not wind speed is similar to the approaches of, e.g., 15 Krings et al. (2011) or Nassar et al. (2017).

For a hydrostatic atmosphere with a standard surface pressure of 1013hPa, n_e is about $2.16 \cdot 10^{25} \text{ cm}^{-2}$ and the cross-sectional CO₂ flux F_{CO_2} (Eq. 2) in units of MtCO₂/a becomes approximately

$$F_{\text{CO}_2} \approx 0.53 \frac{\text{MtCO}_2}{\text{a}} \frac{a_4}{\text{km}} \frac{a_7}{\text{ppm}} \frac{v_e}{\text{m/s}} \quad (3)$$

20

given that the FWHM a_4 , the amplitude of the XCO₂ enhancement a_7 , and the effective wind speed v_e are provided in the units km, ppm, and m/s, respectively. As n_e approximately scales with the surface pressure, Eq. 3 may be easily adapted to other meteorological conditions.

25 As discussed by Brunner et al. (2019), the plume height (and subsequently the wind speed in plume height) depends on many aspects like emission height, stack geometry, flue gas exit velocity and temperature, meteorological conditions, etc. Some of these parameters are not known for many sources and their explicit consideration would go beyond the scope of this study focusing on demonstrating the benefits of simultaneous NO₂ and XCO₂ measurements rather than on most accurate flux estimates. Varon et al. (2018) proposed to approximate the effective wind speed within the plume from the 10 m wind by 30 applying a multiplier in the range of 1.3–1.5. Therefore, we decided to use a multiplier of 1.4 for convenience. This empirical relationship accounts, e.g., for plume rise and mixing into altitudes with larger wind speeds. For the present, we consider this

approximation adequate for this first study, but we recognize that uncertainties (see next section) resulting from this estimate of the effective wind speed's normal may be reduced in the future by improved wind knowledge.

Additionally, it shall be noted that the plume cross-sectional flux (Eq. 2) is only a good approximation for the actual source emission under steady state (temporally invariant) conditions for wind speeds greater than about 2 m/s (Varon et al., 2018) 5 when advection dominates over diffusion (Sharan et al., 1996). Changes in wind direction, wind speed, or atmospheric stability in the time span between emission and observation may result in differences between the plume cross-sectional flux and the source flux. Temporal variations in the source emissions of course also result in (temporally delayed) variations of the plume cross-sectional flux, which is always only a snap shot and must not be confused with, e.g., the annual average, even though given in the same units. In case of chemically active species (such as NO₂), also chemical processes along the plume path 10 would have to be considered in order to compute source emissions from plume cross-sectional fluxes.

2.6 Uncertainty propagation

In order to estimate the uncertainty of the CO₂ plume cross-sectional flux (F_{CO_2} , Eq. 2), we propagate the uncertainties of the FWHM (a_4), the amplitude (a_7), and the wind speed normal (v_e) by assuming uncorrelated errors. The uncertainties of the FWHM and the amplitude result from the maximum likelihood fitting method propagating the uncertainties of the individual 15 XCO₂ and NO₂ soundings as reported in the data products. The uncertainties of the wind components are read from the ECMWF ERA5 data archive resulting in total wind speed uncertainties ranging from 0.18 m/s to 0.33 m/s for the analyzed scenarios. Additionally, we assume that the manual adjustment of the wind direction is accurate by $\pm 10^\circ$. These uncertainties propagate into the uncertainty of the wind speed normal. Varon et al. (2018) estimated that computing the effective wind speed from the 10 m wind introduces an additional uncertainty of 8-12%. However, we analyze scenarios with larger plume 20 structures and probably also larger variations of the injection heights which we consider by enhancing this error component to 20% for convenience. Uncertainties in the number of dry air particles are neglected as they are much smaller compared to, e.g., the wind speed uncertainty. As mentioned earlier, the assumption of constant meteorological conditions might not be valid in regions with large variations of the surface elevation or wind conditions within the plume's cross-section, which may result in an underestimation of the total cross-sectional flux uncertainty in such cases.

25 2.7 Plume detection and scenario selection

We use a semi-automatic method to select potentially interesting targets. In a first step, all co-locations of OCO-2 and S5P are computed similarly as described in section 2.3 but based on a coarser high resolution grid ($0.01^\circ \times 0.01^\circ$) to improve the computational efficiency. We shift a 30 s (~ 200 km) search window in time steps of 0.25 s (~ 2 km) over the time series of co-locations. Only those time steps are further considered which have at least 100 co-locations without data gaps exceeding 30 3 s (~ 20 km) within the search window. In the next step, we perform a least squares fit of the co-located XCO₂ and NO₂ data with a Gaussian vector function. This fitting function corresponds to Eq. 1 but with independent FWHM for XCO₂ and NO₂ and centered within the search window (a_3 and a_8 set to zero), which improves the convergence rate. Only those time steps are further considered fulfilling the following criteria: the fit converged, the NO₂ amplitude exceeds 10^{15} molec./cm², the

Table 1. Summary of cross-sectional flux results including uncertainty contributions (1σ) and comparison with emission data bases EDGAR and ODIAC or GFED in the case of the Australian wildfires. The ODIAC values in brackets represent ODIAC emissions of 2016 and the month of the overpass in the same grid boxes as summed up for 2012. Note that the cross-sectional flux results correspond to the instantaneous time of the overpass' whilst EDGAR and ODIAC emissions are annual or monthly averages; GFED emissions correspond to six hourly averages (see Sec. 2.4). The uncertainty estimate comprises the total uncertainty and the uncertainties introduced by the ECMWF wind uncertainty, the uncertainty of the wind direction (10°), use of the 10 m wind (20%), the XCO₂ precision as reported in the data product, and the NO₂ precision as reported in the data product. All values are in units of MtCO₂/a.

| Emission source | Cross-sect. flux | Cross-sectional flux uncertainty | | | | | | EDGAR | ODIAC/ GFED* |
|-----------------------|---------------------|----------------------------------|-------|-------|------|------------------|-----------------|-------|-----------------|
| | | Total | ECMWF | Angle | 10 m | XCO ₂ | NO ₂ | | |
| Moscow | 76 | 33 | 4 | 29 | 15 | 5 | 1 | 195 | 102 (88) |
| Lipetsk | 69 | 50 | 5 | 48 | 14 | 1 | 0 | 23 | 4 (4) |
| Baghdad | 95 | 36 | 3 | 30 | 19 | 6 | 1 | 22 | 13 (12) |
| Medupi and Matimba | 31 | 7 | 3 | 2 | 6 | 2 | 0 | 0 | 24 (26) |
| Australian wildfires* | 153 | 40 | 5 | 24 | 31 | 8 | 5 | 0 | 52 |
| Nanjing | 120 | 27 | 10 | 5 | 24 | 6 | 1 | 164 | 89 (96) |

XCO₂ and NO₂ FWHM (a_c and a_n , respectively) do not exceed the half width of the search window ($a_c, a_n \leq 15 s$) and do not differ by more than their average ($|a_c - a_n| \leq (a_c + a_n)/2$), the XCO₂ and NO₂ amplitudes are at least two times larger than their uncertainties and larger than the maximum variations of the backgrounds. In the last step, we decided by manual inspection of the XCO₂ and NO₂ co-locations plus the surrounding NO₂ fields and ECMWF wind information if the scenario 5 is a promising candidate for further flux analyses. Potential reasons to reject an automatically pre-selected scenario are, e.g., too low wind speed, wind direction nearly parallel to OCO-2 orbit, unclear source attribution, or poor fit quality. In total, we manually identified about 20 promising scenarios in the time period 01/2018 to 08/2018 of which we selected and analyzed six examples for this study.

3 Results

10 From the time period of 01/2018 to 08/2018, we selected the following scenarios as examples for flux analyses based on co-located XCO₂ and NO₂ observations.

3.1 Moscow

Fig. 1a shows the NO₂ enhancement in the city plume of Moscow (approx. 12.4 million inhabitants) as retrieved from S5P overlaid by OCO-2's XCO₂ measurements. The NO₂ enhancement is clearly visible also in the plume's cross-section along 15 OCO-2's ground track (Fig. 1c). Due to the larger relative noise of the XCO₂ retrievals, the XCO₂ enhancement is less obvious but still visible (Fig. 1c). The Gaussian fit of the enhancements is excellent for NO₂ and reasonable ($\chi^2 = 2.2$) for XCO₂.

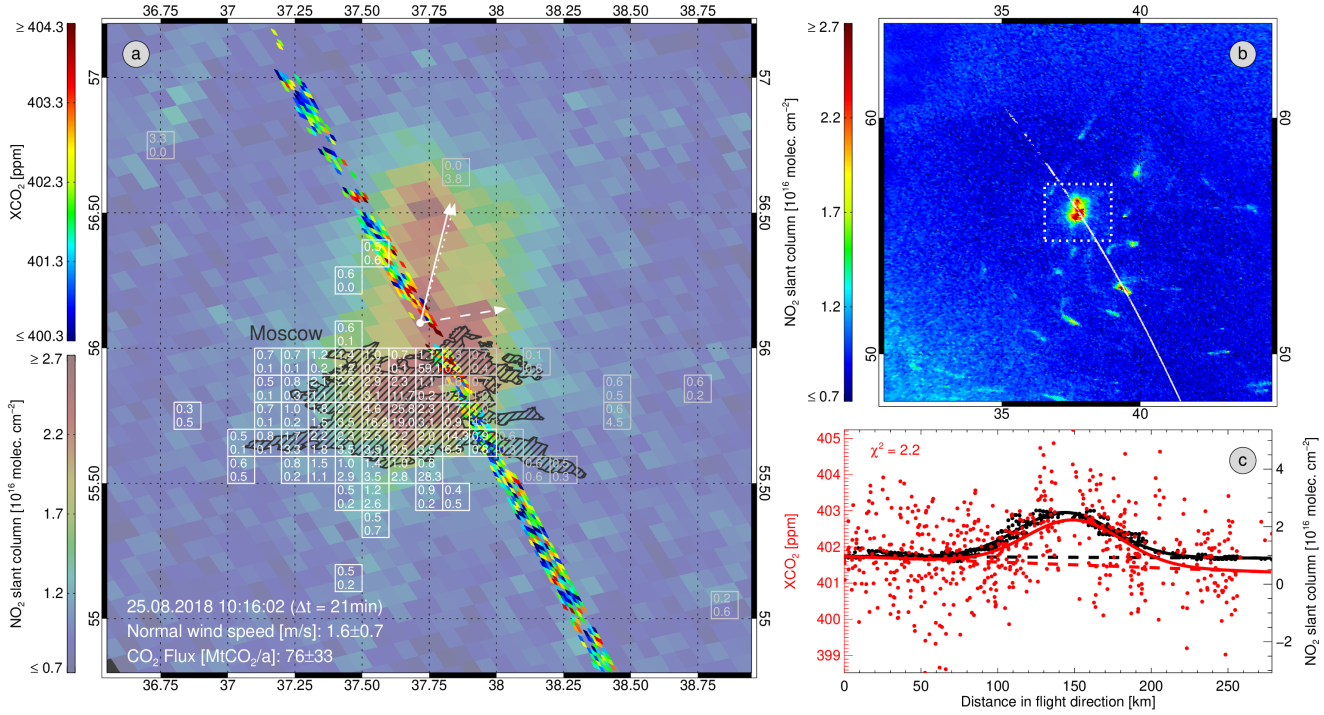


Figure 1. Moscow on August 25, 2018. **a)** S5P NO₂ slant column (background) overlayed by OCO-2 XCO₂ (foreground). Gray and white 0.1° boxes show EDGAR (bottom) and ODIAC (top) 2012 annual emissions with either EDGAR or ODIAC being larger than 0.5 MtCO₂/a. The white arrows show the direction of the 10 m wind as read from ECMWF (dotted), manually corrected to (subjectively) best match the NO₂ plume (solid), and normal to the OCO-2 orbit (dashed). Effective wind speed normal to the OCO-2 orbit, estimated cross-sectional CO₂ flux, time of OCO-2 overpass, and time difference between OCO-2 and S5P overpass are also listed. The hatched area corresponds to the urban area (World Urban Areas dataset, Geoportal of the University of California, https://apps.gis.ucla.edu/geodata/dataset/world_urban_areas). **b)** Larger section of the S5P NO₂ slant columns including the OCO-2 orbit and the bounding box of sub-figure a). **c)** OCO-2 XCO₂ values (red) and co-located S5P NO₂ slant columns (black) within the plume's cross-section in OCO-2 flight direction.

There was nearly no adjustment needed (1°) to bring the ECMWF 10 m wind in good agreement with the NO₂ plume (Fig. 1a). The effective wind speed normal to the OCO-2 orbit amounts to 1.6 ± 0.6 m/s which is a bit lower than optimal for reasonable flux estimates (Varon et al., 2018). The cross-sectional CO₂ flux amounts to 76 ± 33 MtCO₂/a. This compares to 2012 average upwind emissions (white marked boxes in Fig. 1a) of 195 MtCO₂/a (EDGAR) and 102 MtCO₂/a (ODIAC). ODIAC's emission estimate for 08/2016 amounts to 88 MtCO₂/a. The NO₂ far field shows no indications for overlayed CO₂ plumes from other sources (Fig. 1b). The total flux uncertainty is dominated by the uncertainty of the wind direction followed by the uncertainty of the effective wind speed.

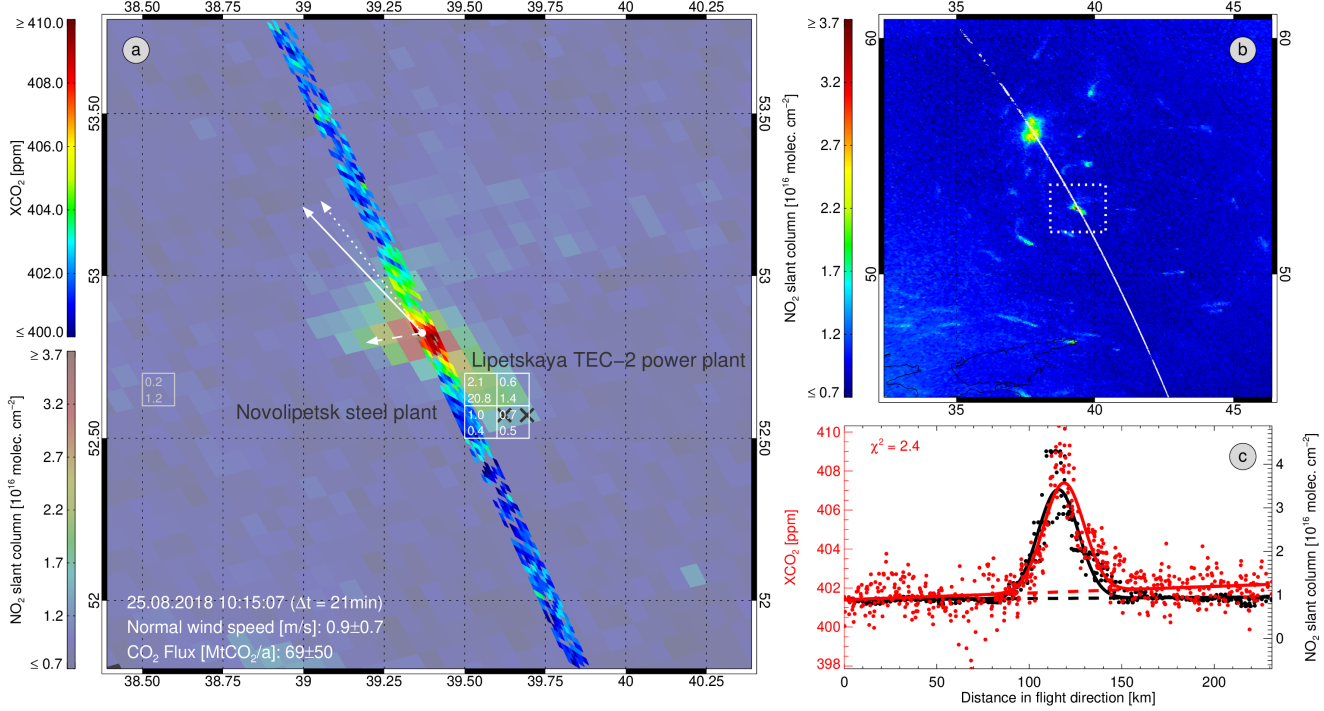


Figure 2. As Fig. 1 but for Lipetsk on August 25, 2018.

3.2 Lipetsk

Fig. 2a shows the surrounding of Lipetsk (approx. 0.5 million inhabitants) with, among other industries, the Novolipetsk steel plant and the Lipetskaya TEC-2 gas-fired power plant (515MW) only one minute (~ 400 km) apart from Moscow along OCO-2's flight track (see also Fig. 1b). The cross-sectional NO_2 and XCO_2 enhancements clearly stand out of the noise of the data (Fig. 2c) and the Gaussian function fits the XCO_2 data reasonably well ($\chi^2 = 2.4$). We applied a small correction of 5° to the ECMWF wind direction. However, as the wind direction is similar to OCO-2's flight direction, the normal effective wind speed is unfavorably low (0.9 ± 0.7 m/s) which makes the cross-sectional flux estimates (69 ± 50 Mt CO_2 /a) less reliable and highly uncertain. The by far largest uncertainty contribution comes from the uncertainty of the wind direction. The 2012 average EDGAR and ODIAC upwind emissions (white marked boxes in Fig. 2a) are 23 Mt CO_2 /a and 4 Mt CO_2 /a (same for 08/2016), respectively, but the NO_2 far field shows no indications for overlayed CO_2 plumes from other sources (Fig. 2b).

3.3 Baghdad

Fig. 3a shows the S5P NO_2 slant columns overlaid by OCO-2 XCO_2 data in a surrounding of Baghdad (approx. 5.4 million inhabitants). Enhanced values are clearly visible in the cross-section of the NO_2 plume and less obviously visible also in the XCO_2 data (Fig. 3c). The XCO_2 enhancement is well fitted ($\chi^2 = 1.0$) by the Gaussian fitting function. The manually adjusted

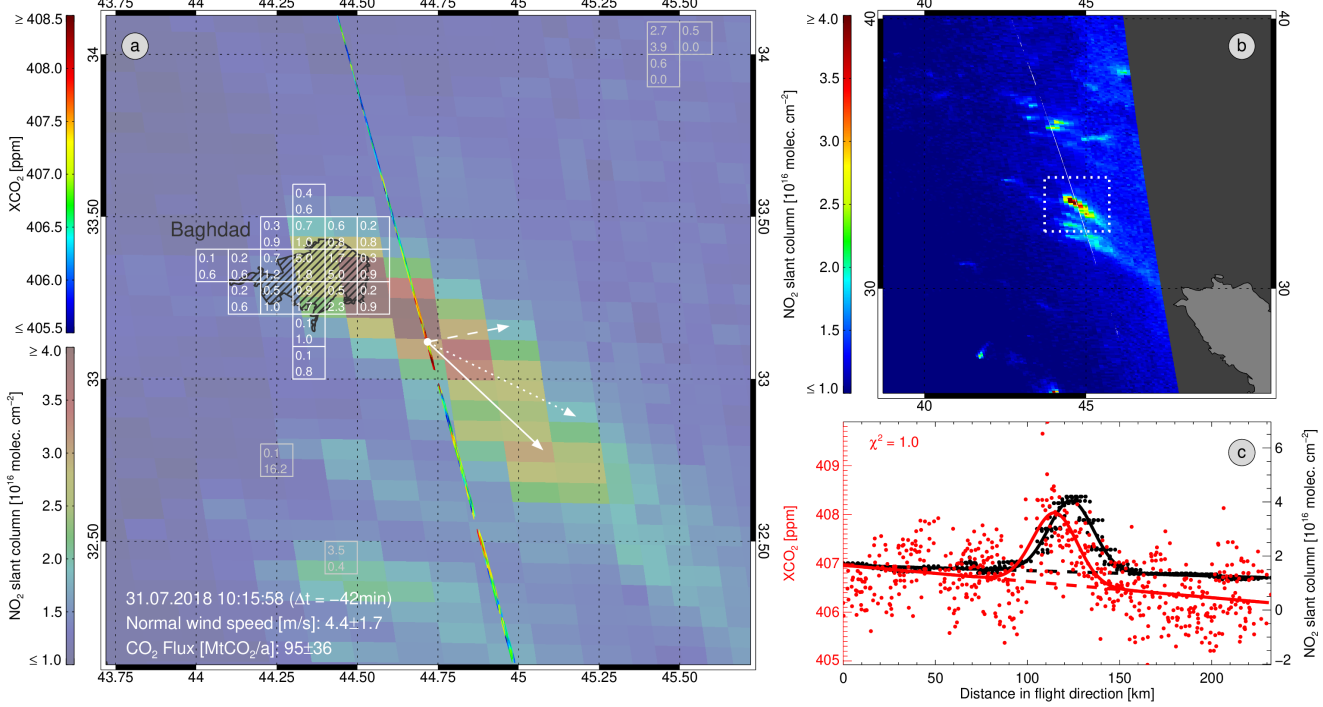


Figure 3. As Fig. 1 but for Baghdad on July 31, 2018.

wind direction deviates by 17° from the ECMWF wind direction and the normal wind speed amounts to 4.4 ± 1.7 m/s. From the XCO₂ enhancement and the normal wind speed, we compute the cross-sectional CO₂ flux to be 95 ± 36 MtCO₂/a. This compares to an upwind source of 22 MtCO₂/a or 13 MtCO₂/a (12 MtCO₂/a for 07/2016) of EDGAR or ODIAC, respectively. The flux uncertainty is dominated by the uncertainty of the wind direction and the uncertainty of the effective wind speed.

5 NO₂ far field shows no indications for overlayed CO₂ plumes from other sources (Fig. 3b).

3.4 Medupi and Matimba power plants

The Medupi (4764MW) and Matimba (3990MW) coal-fired power plants lie close to each other in South Africa about 300 km north of Johannesburg. Their NO₂ plume is shown in Fig. 4a overlaid by OCO₂ XCO₂ measurements. NO₂ measurements in the larger surrounding do not suggest any additional nearby upwind sources (Fig. 4b). The cross-sectional NO₂ values show a clear elevation within the plume which is less obvious for XCO₂ having larger relative scatter especially south of the plume. Nevertheless, the Gaussian function fits the XCO₂ values reasonably well ($\chi^2 = 1.4$). The wind direction (corrected by 13°) is nearly perpendicular to the OCO-2 orbit and the effective normal wind speed is 2.6 ± 0.6 m/s. The cross-sectional CO₂ flux amounts to 31 ± 7 MtCO₂/a which is consistent with ODIAC 2012 emissions of 24 MtCO₂/a and ODIAC 07/2016 emissions of 26 MtCO₂/a but EDGAR does not have significant emissions in this area. It shall be noted that the Medupi power plant started 10 operation in 2015 with limited capacity and that it still has not reached its nominal capacity. Therefore, it is no surprise that 15

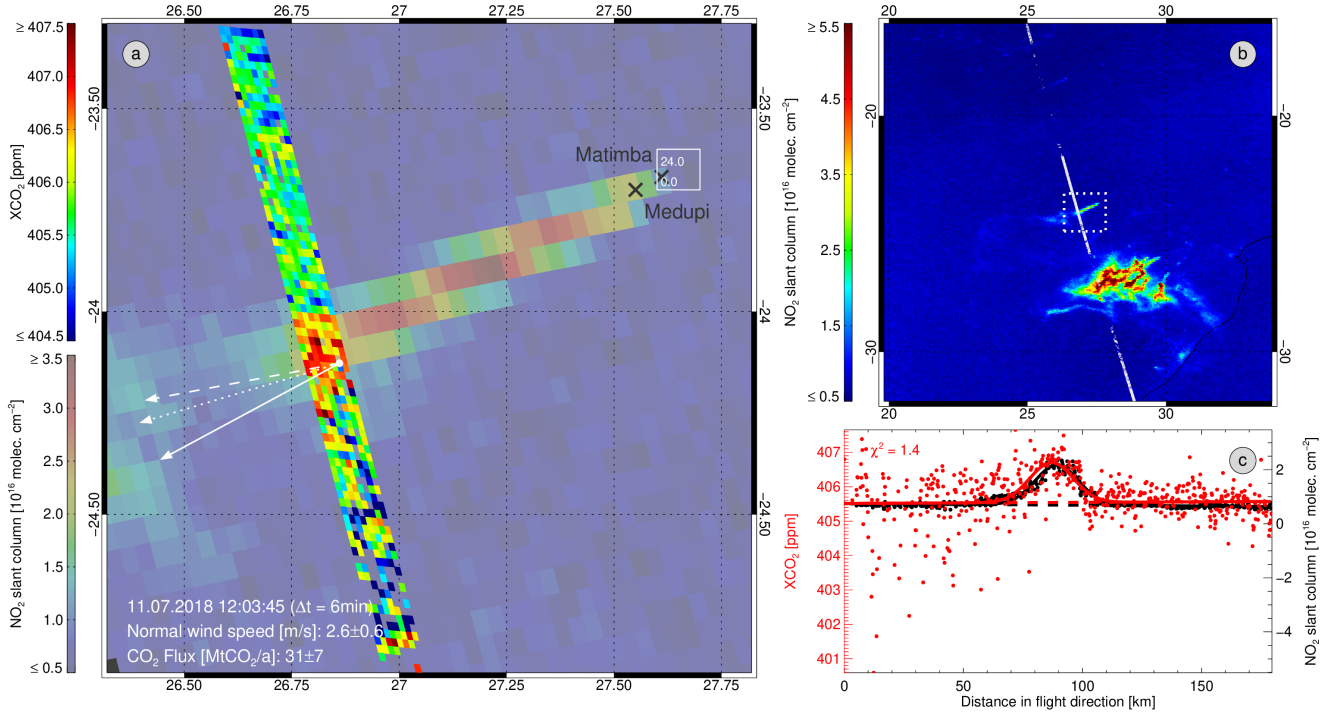


Figure 4. As Fig. 1 but for the Medupi and Matimba power plants in South Africa on July 11, 2018.

the Medupi power station is not included in either EDGAR or ODIAC 2012 data. The flux uncertainty is dominated by the uncertainty of the effective wind speed.

3.5 Australian wildfires

Fig. 5a shows the NO_2 plumes of two Australian wildfires on 05.05.2018 overlaid by an OCO-2 orbit of XCO_2 measurements. 5 Enhanced NO_2 and XCO_2 values are clearly visible within the plume's cross-section (Fig. 5b). The NO_2 (and less obvious also the XCO_2) cross-section has two maxima which cannot be accounted for by the Gaussian fitting function. However, this is not reflected in the good XCO_2 fit quality ($\chi^2 = 0.6$), but should be taken into account when valuing the results. We applied a small manual correction of 7° to the wind direction and the effective wind speed normal to the OCO-2 orbit is 6.7 ± 1.7 m/s. For the snapshot of the overpass, we computed a cross-sectional CO_2 flux of 153 ± 40 Mt CO_2 /a. Its uncertainty is driven by 10 the uncertainty of the effective wind speed and wind direction. As the shown plumes originate from wildfires, EDGAR and ODIAC do not include their emissions. However, GFED has average emissions of 52 Mt CO_2 /a within the six hours period 0h–6h UTC including the time of the overpass (5h UTC). The maximum GFED emissions are approximately at the position of the largest NO_2 concentrations. Fig. 5c shows no indications, that additional upwind sources may explain the discrepancy between our cross-sectional flux estimate and GFED.

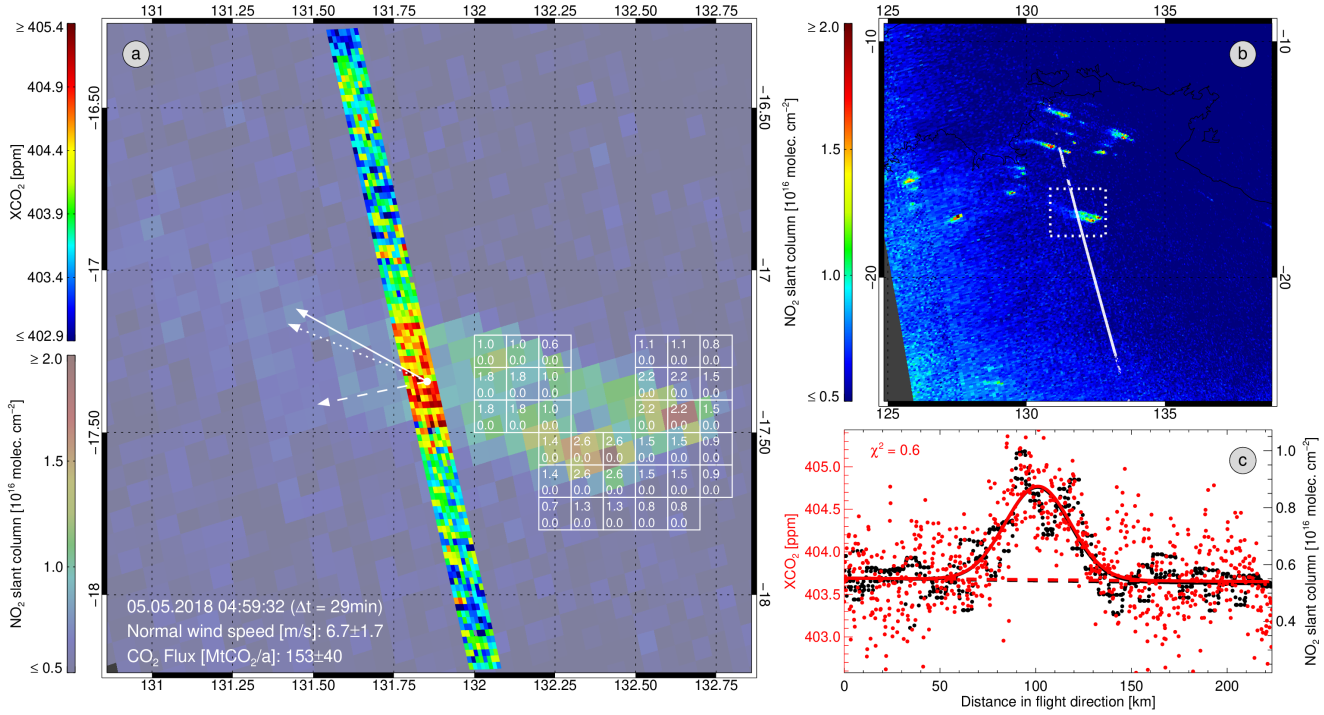


Figure 5. As Fig. 1 but for Australian wildfires on May 5, 2018. The ODIAC emission data (top number) have been replaced by GFED emissions for the time of the OCO-2 overpass.

3.6 Nanjing

Fig. 6a shows the NO₂ slant columns in the surrounding of Nanjing (approx. 5.8 million inhabitants) overlaid by OCO-2 XCO₂ measurements. The cross-section along the OCO-2 orbit shows strong XCO₂ and NO₂ plume signals distinctively above the noise level which are well fitted with the Gaussian fitting function ($\chi^2 = 0.6$). The ECMWF wind direction is not far from being rectangular to the OCO-2 orbit and we applied a moderate manual correction of 11°. The effective normal wind speed is 2.2 ± 0.5 m/s. This results in a cross-sectional flux estimate of 120 ± 27 MtCO₂/a which lies in between the upwind emissions of EDGAR (163 MtCO₂/a) and ODIAC (89 MtCO₂/a for 2012, 96 MtCO₂/a for 03/2016). Fig. 6b does not indicate additional major remote upwind sources. The uncertainty of the cross-sectional flux estimate is dominated by the uncertainty of the effective wind speed.

10 4 Discussion and conclusions

Based on six case studies (Moscow, Russia; Lipetsk, Russia; Baghdad, Iraq; Medupi and Matimba power plants, South Africa; Australian wildfires; and Nanjing, China), we demonstrated the usefulness of simultaneous satellite observations of NO₂ and the column-average dry-air mole fraction of CO₂ (XCO₂). For this purpose, we analyzed co-located regional enhancements of

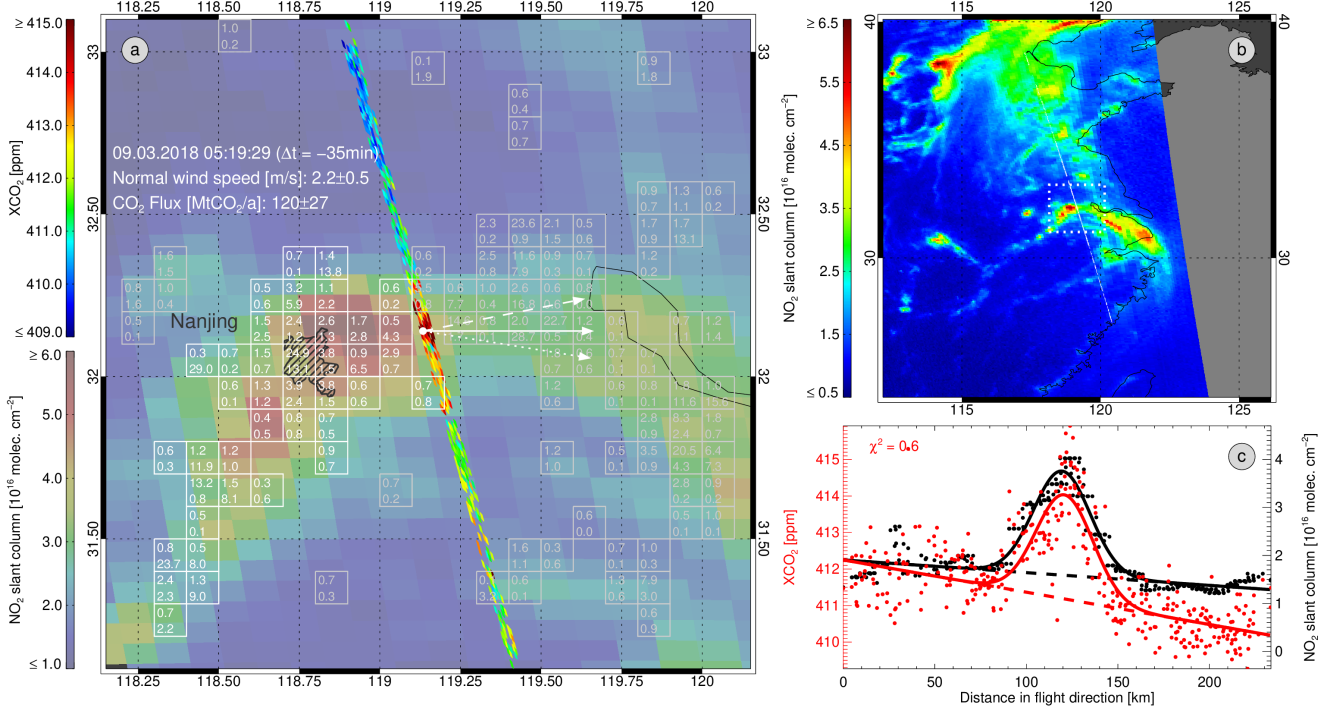


Figure 6. As Fig. 1 but for Nanjing on March 9, 2018.

XCO₂ observed by OCO-2 and NO₂ from S5P and estimated the CO₂ plume's cross-sectional fluxes. For atmospheric standard conditions, we approximated as a rule of thumb, that a Gaussian enhancement of 1 ppm with a width of 1 km at a wind speed (normal to the cross-section) of 1 m/s corresponds to a plume cross-sectional flux of roughly 0.53 MtCO₂/a.

For Moscow, we derived a cross-sectional flux of 76±33 MtCO₂/a which agrees (within its uncertainty) with ODIAC 2012 emissions of 102 MtCO₂/a (88 MtCO₂/a for 08/2016) but not with EDGAR emissions of 195 MtCO₂/a. The cross-sectional flux estimate of Lipetsk with the Novolipetsk steel plant and the Lipetskaya TEC-2 power plant is 69±50 MtCO₂/a. Within its uncertainty, this estimate agrees with EDGAR emissions of 23 MtCO₂/a but not with ODIAC emissions of 4 MtCO₂/a. However, the uncertainty of the estimate is large due to a wind direction with an acute angle relative to the OCO-2 orbit which also results in a low effective normal wind speed. This can serve as an example for low wind speeds being favorable for plume detection but not necessarily for flux quantification. In the case of Baghdad, we derived a cross-sectional flux of 95±36 MtCO₂/a for the time of the overpass which is considerably larger than the annual average EDAGR (22 MtCO₂/a) and ODIAC (13 MtCO₂/a for 2012, 12 MtCO₂/a for 07/2016) emissions of 2012. The wind conditions were relatively good and S5P NO₂ measurements do not suggest an overlaying significant upwind source. In this context, it is interesting to note that Georgoulias et al. (2019) found a strongly increasing trend (17.0±0.8%/a in the period 04/1996–09/2017) for the tropospheric NO₂ concentrations in Baghdad (and a decreasing trend of -2.2±0.7%/a for Iraq) hinting at strongly increasing CO₂ emissions in Baghdad since 2012. The cross-sectional flux of the plume of the Medupi and Matimba power plants have been estimated

to 31 ± 7 MtCO₂/a which agrees (within its uncertainty) with ODIAC (24 MtCO₂/a for 2012, 26 MtCO₂/a for 07/2016) but not with EDGAR (no significant emission). Nassar et al. (2017) also estimated the emissions from the Matimba power plant (but not Medupi) using OCO-2 XCO₂ v7 data. For a direct overpass in 2014 and a close flyby (~ 7 km away) in 2016 they found fluxes, converted to annual values, of 12.1 ± 3.9 MtCO₂/a and 12.3 ± 1.2 MtCO₂/a, respectively. For the Australian wildfires, 5 we estimated a plume cross-sectional flux of 153 ± 40 MtCO₂/a which is about three times larger than the GFED estimate (52 MtCO₂/a) for a six hours average ending approximately at the time of the OCO-2 overpass. Unfavorable wind conditions or a strong overlaying upwind source can be excluded as reason for the discrepancy. The same is true for the fact that a double-plume structure has been fitted with a Gaussian function. However, it shall be noted that GFED's emission estimate for the 10 same time interval but one day before the OCO-2 overpass amounts to 252 MtCO₂/a. For the Nanjing scenario, we derived a cross-sectional flux of 120 ± 27 MtCO₂/a which lies in between ODIAC (89 MtCO₂/a for 2012, 96 MtCO₂/a for 03/2016) and EDGAR (164 MtCO₂/a). However, the scene includes a larger area of overlaying sources, making source attribution difficult.

The total uncertainty of the derived plume cross-sectional fluxes ranges from 7 MtCO₂/a to 50 MtCO₂/a or in relative measures from 23% to 72%. The total uncertainty is always dominated by an uncertainty contribution related to meteorology. Specifically, the (manually adjusted) wind direction or the computation of the effective wind speed from the 10 m wind 15 contribute most to the total uncertainty. The noise of the XCO₂ retrievals contributes only with 1 MtCO₂/a to 8 MtCO₂/a to the total error and the noise of the NO₂ retrievals contributes on average even three times less.

It is unlikely, that the observed XCO₂ enhancements are dominated by uncorrected enhancements due to co-emitted aerosols because the OCO-2 retrieval algorithm accounts for light scattering at optically thin aerosol layers and filters scenes with stronger aerosol contamination. Additionally, Bovensmann et al. (2010) estimated for the proposed CarbonSat (Carbon Monitoring Satellite) instrument that neglecting co-emitted aerosols in power plant plumes results in errors between 0.2 MtCO₂/a and 2.5 MtCO₂/a which is small compared with the derived cross-sectional fluxes and their total uncertainties (Tab. 1). Aerosols can also effect the S5P NO₂ slant columns which is, however, less important for our work because we derive only the plume width and direction from the NO₂ observations.

It shall be noted that differences of the cross-sectional flux estimates and the emission data bases are not necessarily coming 25 from inaccuracies of the satellite retrievals or the emission data bases. Our estimates are valid only for the time of the overpass while the emission data bases give annual or monthly averages. Velazco et al. (2011) illustrated, that power plants can have substantial annual and day-to-day variations. Additionally, the cross-sectional flux is only a good approximation for the source emission under meteorological steady state conditions with wind speeds greater than about 2 m/s (Varon et al., 2018).

For the analyzed scenarios, we observe rather large differences between the EDGAR and ODIAC emission inventories. However, note that only those grid boxes are shown (and summed up) in Fig. 1a–6a for which either EDGAR or ODIAC emissions 30 are larger than 0.5 MtCO₂/a. This means, a smoother distribution of emissions may be misinterpreted as less emissions, if a significant fraction of the total emission is located in grid boxes not exceeding the 0.5 MtCO₂/a threshold. Additionally, it shall be noted that ODIAC emissions correspond to fossil fuel combustion and cement production only, while EDGAR includes also emissions from other sectors (e.g., agriculture, land use change, and waste).

NO₂ is co-emitted with CO₂ when fossil fuels are combusted at high temperatures and has a relatively short lifetime of the order of hours which makes it a suitable tracer for recently emitted CO₂. Despite less strict quality filtering is needed, plume enhancements of NO₂ columns near sources can be retrieved from satellites with much lower relative noise than this is the case for XCO₂. We take advantage of these points by using NO₂ measurements to i) identify the source of the observed XCO₂ 5 enhancements, ii) to exclude interference with potential additional remote upwind sources, iii) to manually adjust the wind direction, and iv) to put a constraint on the shape of the observed CO₂ plumes.

In principle, it is also possible, to fit only the XCO₂ values without constraining the plume shape by NO₂. In this case, XCO₂ is used to derive the amplitude and FWHM of the enhancement. We repeated the flux estimation of all shown scenarios with such a setup and got fluxes of 61 ± 27 MtCO₂/a, 63 ± 46 MtCO₂/a, 75 ± 29 MtCO₂/a, 35 ± 9 MtCO₂/a, 166 ± 44 MtCO₂/a, 10 and 119 ± 28 MtCO₂/a for the Moscow, Lipetsk, Baghdad, Medupi/Matimba, Australian wildfires, and Nanjing scenario, respectively. The derived fluxes are consistent within their uncertainty with our main results shown in Tab. 1, but the uncertainty contribution due to the noise in the XCO₂ data increased by 34% from 4.7 MtCO₂/a to 6.3 MtCO₂/a on average.

Reuter et al. (2014) discussed that post-ENVISAT missions such as OCO-2 would benefit from co-located measurements of co-emitted species from other satellites or ideally multi-species measurements from the same instrument. We demonstrated, 15 that the analysis of small scale emissions in OCO-2 XCO₂ data indeed profits from simultaneous NO₂ observations of S5P as they allow to set the XCO₂ observations into context but also to constrain the plume structure. The uncertainties of the cross-sectional flux estimates due to meteorology and their agreement with the actual emissions might be improved in subsequent studies by making use of dedicated simulations with Lagrangian particle dispersion models with either known source positions (and injection heights) or source positions inferred from the NO₂ data.

20 However, we expect the largest room for improvements in satellite missions such as the planned European Copernicus anthropogenic CO₂ monitoring mission (CO2M) which will provide not only precise measurements with high spatial resolution but also imaging capabilities with a wider swath of simultaneous XCO₂ and NO₂ observations. Its imaging capabilities will reduce the uncertainty of the inferred emissions due to measurement noise simply because of the increased number of soundings. Additionally, simultaneous XCO₂ and NO₂ observations from the same platform will allow stricter constraints on the 25 plume shape. More importantly, the meteorology related uncertainties will reduce (Varon et al., 2018) because deviations from steady state conditions can average out and are, therefore, less critical if the entire plume structure is sampled rather than only a cross-section.

Author contributions. M.R.: experimental set-up, data analysis, interpretation, writing the paper. M.B., O.S., S.K., H.B., J.P.B.: experimental set-up, interpretation, improving the paper. A.R.: interpretation, design and operation of the NO₂ satellite retrieval, improving the paper. 30 C.W.O'D.: interpretation, design and operation of the XCO₂ satellite retrieval, improving the paper.

Competing interests. The authors declare that they have no conflict of interest.

Acknowledgements. This work was funded by the State and the University of Bremen. The OCO-2 XCO₂ data were produced by the OCO-2 project at the Jet Propulsion Laboratory, California Institute of Technology, and obtained from the OCO-2 data archive maintained at the NASA Goddard Earth Science Data and Information Services Center. This publication contains modified Copernicus Sentinel data (2018). S5P is an ESA mission implemented on behalf of the European Commission. The TROPOMI payload is a joint development by ESA and the Netherlands Space Office (NSO). The S5P ground-segment development has been funded by ESA and with national contributions from The Netherlands, Germany, and Belgium. ERA5 meteorological profiles have been obtained from the Copernicus Climate Change Service (C3S) operated by ECMWF. CO₂ emission data have been obtained from the EDGAR, ODIAC, and the GFED data bases.

References

Boersma, K., Eskes, H., Veefkind, J., Brinksma, E., Van Der A, R., Sneep, M., Van Den Oord, G., Levelt, P., Stammes, P., Gleason, J., et al.: Near-real time retrieval of tropospheric NO₂ from OMI, *Atmospheric Chemistry and Physics*, 7, 2103–2118, 2007.

Bovensmann, H., Burrows, J. P., Buchwitz, M., Frerick, J., Noël, S., Rozanov, V. V., Chance, K. V., and Goede, A.: SCIAMACHY – Mission Objectives and Measurement Modes, *Journal of the Atmospheric Sciences*, 56, 127–150, [http://dx.doi.org/10.1175/1520-0469\(1999\)056<0127:SMOAMM>2.0.CO;2](http://dx.doi.org/10.1175/1520-0469(1999)056<0127:SMOAMM>2.0.CO;2), 1999.

Bovensmann, H., Buchwitz, M., Burrows, J. P., Reuter, M., Krings, T., Gerilowski, K., Schneising, O., Heymann, J., Tretner, A., and Erzinger, J.: A remote sensing technique for global monitoring of power plant CO₂ emissions from space and related applications, *Atmospheric Measurement Techniques*, 3, 781–811, <https://doi.org/10.5194/amt-3-781-2010>, <http://www.atmos-meas-tech.net/3/781/2010/>, 2010.

Brunner, D., Kuhlmann, G., Marshall, J., Clément, V., Fuhrer, O., Broquet, G., Löscher, A., and Meijer, Y.: Accounting for the vertical distribution of emissions in atmospheric CO₂ simulations, *Atmospheric Chemistry and Physics*, 19, 4541–4559, 2019.

Buchwitz, M., Schneising, O., Reuter, M., Heymann, J., Krautwurst, S., Bovensmann, H., Burrows, J. P., Boesch, H., Parker, R. J., Somkuti, P., Detmers, R. G., Hasekamp, O. P., Aben, I., Butz, A., Frankenberg, C., and Turner, A. J.: Satellite-derived methane hotspot emission estimates using a fast data-driven method, *Atmospheric Chemistry and Physics*, 17, 5751–5774, <https://doi.org/10.5194/acp-17-5751-2017>, <https://www.atmos-chem-phys.net/17/5751/2017/>, 2017.

Burrows, J. P., Höhlzle, E., Goede, A. P. H., Visser, H., and Fricke, W.: SCIAMACHY – Scanning Imaging Absorption Spectrometer for Atmospheric Chartography, *Acta Astronautica*, 35, 445–451, 1995.

Ciais, P., Dolman, A. J., Bombelli, A., Duren, R., Peregon, A., Rayner, P. J., Miller, C., Gobron, N., Kinderman, G., Marland, G., Gruber, N., Chevallier, F., Andres, R. J., Balsamo, G., Bopp, L., Bréon, F.-M., Broquet, G., Dargaville, R., Battin, T. J., Borges, A., Bovensmann, H., Buchwitz, M., Butler, J., Canadell, J. G., Cook, R. B., DeFries, R., Engelen, R., Gurney, K. R., Heinze, C., Heimann, M., Held, A., Henry, M., Law, B., Luyssaert, S., Miller, J., Moriyama, T., Moulin, C., Myneni, R. B., Nussli, C., Obersteiner, M., Ojima, D., Pan, Y., Paris, J.-D., Piao, S. L., Poulter, B., Plummer, S., Quegan, S., Raymond, P., Reichstein, M., Rivier, L., Sabine, C., Schimel, D., Tarasova, O., Valentini, R., Wang, R., van der Werf, G., Wickland, D., Williams, M., and Zehner, C.: Current systematic carbon-cycle observations and the need for implementing a policy-relevant carbon observing system, *Biogeosciences*, 11, 3547–3602, <https://doi.org/10.5194/bg-11-3547-2014>, <http://www.biogeosciences.net/11/3547/2014/>, 2014.

Crisp, D., Atlas, R. M., Bréon, F.-M., Brown, L. R., Burrows, J. P., Ciais, P., Connor, B. J., Doney, S. C., Fung, I. Y., Jacob, D. J., Miller, C. E., O'Brien, D., Pawson, S., Randerson, J. T., Rayner, P., Salawitch, R. S., Sander, S. P., Sen, B., Stephens, G. L., Tans, P. P., Toon, G. C., Wennberg, P. O., Wofsy, S. C., Yung, Y. L., Kuang, Z., Chudasama, B., Sprague, G., Weiss, P., Pollock, R., Kenyon, D., and Schroll, S.: The Orbiting Carbon Observatory (OCO) mission, *Advances in Space Research*, 34, 700–709, 2004.

Georgoulias, A. K., van der A, R. J., Stammes, P., Boersma, K. F., and Eskes, H. J.: Trends and trend reversal detection in 2 decades of tropospheric NO₂ satellite observations, *Atmospheric Chemistry and Physics*, 19, 6269–6294, <https://doi.org/10.5194/acp-19-6269-2019>, <https://www.atmos-chem-phys.net/19/6269/2019/>, 2019.

Heymann, J., Reuter, M., Buchwitz, M., Schneising, O., Bovensmann, H., Burrows, J., Massart, S., Kaiser, J., and Crisp, D.: CO₂ emission of Indonesian fires in 2015 estimated from satellite-derived atmospheric CO₂ concentrations, *Geophysical Research Letters*, 44, 1537–1544, 2017.

Kiel, M., O'Dell, C. W., Fisher, B., Eldering, A., Nassar, R., MacDonald, C. G., and Wennberg, P. O.: How bias correction goes wrong: measurement of XCO₂ affected by erroneous surface pressure estimates, *Atmospheric Measurement Techniques*, 12, 2241–2259, <https://doi.org/10.5194/amt-12-2241-2019>, <https://www.atmos-meas-tech.net/12/2241/2019/>, 2019.

Krings, T., Gerilowski, K., Buchwitz, M., Reuter, M., Tretner, A., Erzinger, J., Heinze, D., Pflüger, U., Burrows, J. P., and Bovensmann, H.: 5 MAMAP - a new spectrometer system for column-averaged methane and carbon dioxide observations from aircraft: retrieval algorithm and first inversions for point source emission rates, *Atmospheric Measurement Techniques*, 4, 1735–1758, <https://doi.org/10.5194/amt-4-1735-2011>, <https://www.atmos-meas-tech.net/4/1735/2011/>, 2011.

Kuze, A., Suto, H., Nakajima, M., and Hamazaki, T.: Thermal and near infrared sensor for carbon observation Fourier-transform spectrometer on the Greenhouse Gases Observing Satellite for greenhouse gases monitoring, *Applied Optics*, 48, 6716, 10 <https://doi.org/10.1364/AO.48.006716>, <http://dx.doi.org/10.1364/AO.48.006716>, 2009.

Nassar, R., Hill, T. G., McLinden, C. A., Wunch, D., Jones, D., and Crisp, D.: Quantifying CO₂ emissions from individual power plants from space, *Geophysical Research Letters*, 44, 2017.

Oda, T., Maksyutov, S., and Andres, R. J.: The Open-source Data Inventory for Anthropogenic CO₂, version 2016 (ODIAC2016): a global monthly fossil fuel CO₂ gridded emissions data product for tracer transport simulations and surface flux inversions, *Earth System Science 15 Data*, 10, 87–107, <https://doi.org/10.5194/essd-10-87-2018>, <https://www.earth-syst-sci-data.net/10/87/2018/>, 2018.

O'Dell, C. W., Eldering, A., Wennberg, P. O., Crisp, D., Gunson, M. R., Fisher, B., Frankenberg, C., Kiel, M., Lindqvist, H., Mandrake, L., Merrelli, A., Natraj, V., Nelson, R. R., Osterman, G. B., Payne, V. H., Taylor, T. E., Wunch, D., Drouin, B. J., Oyafuso, F., Chang, A., McDuffie, J., Smyth, M., Baker, D. F., Basu, S., Chevallier, F., Crowell, S. M. R., Feng, L., Palmer, P. I., Dubey, M., García, O. E., Griffith, D. W. T., Hase, F., Iraci, L. T., Kivi, R., Morino, I., Notholt, J., Ohyama, H., Petri, C., Roehl, C. M., Sha, M. K., Strong, 20 K., Sussmann, R., Te, Y., Uchino, O., and Velazco, V. A.: Improved retrievals of carbon dioxide from Orbiting Carbon Observatory-2 with the version 8 ACOS algorithm, *Atmospheric Measurement Techniques*, 11, 6539–6576, <https://doi.org/10.5194/amt-11-6539-2018>, <https://www.atmos-meas-tech.net/11/6539/2018/>, 2018.

Pinty, B., Janssens-Maenhout, G., M., D., Zunker, H., Brunhes, T., Ciais, P., Denier van der Gon, D. Dee, H., Dolman, H., M., D., Engelen, R., Heimann, M., Holmlund, K., Husband, R., Kentarchos, A., Meijer, Y., Palmer, P., and Scholze, M.: An Operational Anthropogenic CO₂ 25 Emissions Monitoring & Verification Support capacity - Baseline Requirements, Model Components and Functional Architecture, European Commission Joint Research Centre, EUR 28736 EN, <https://doi.org/10.2760/39384>, http://copernicus.eu/sites/default/files/library/Report_Copernicus_CO2_Monitoring_TaskForce_Nov2017.pdf, 2017.

Reuter, M., Buchwitz, M., Hilboll, A., Richter, A., Schneising, O., Hilker, M., Heymann, J., Bovensmann, H., and Burrows, J.: Decreasing emissions of NO_x relative to CO₂ in East Asia inferred from satellite observations, *Nature Geoscience*, 7, 792, 2014.

Reuter, M., Buchwitz, M., Schneising, O., Noël, S., Bovensmann, H., and Burrows, J. P.: A fast atmospheric trace gas retrieval for 30 hyperspectral instruments approximating multiple scattering - Part 2: application to XCO₂ retrievals from OCO-2, *Remote Sensing*, 9, <https://doi.org/10.3390/rs9111102>, <http://www.mdpi.com/2072-4292/9/11/1102>, 2017.

Richter, A., Burrows, J. P., Nüß, H., Granier, C., and Niemeier, U.: Increase in tropospheric nitrogen dioxide over China observed from space, *Nature*, 437, 129–132, <https://doi.org/10.1038/nature04092>, 2005.

Richter, A., Begoin, M., Hilboll, A., and Burrows, J.: An improved NO₂ retrieval for the GOME-2 satellite instrument, *Atmospheric Measurement Techniques*, 4, 1147–1159, 2011.

Rockström, J., Gaffney, O., Rogelj, J., Meinshausen, M., Nakicenovic, N., and Schellnhuber, H. J.: A roadmap for rapid decarbonization, *Science*, 355, 1269–1271, 2017.

Schneising, O., Heymann, J., Buchwitz, M., Reuter, M., Bovensmann, H., and Burrows, J. P.: Anthropogenic carbon dioxide source areas observed from space: assessment of regional enhancements and trends, *Atmospheric Chemistry and Physics*, 13, 2445–2454, <https://doi.org/10.5194/acp-13-2445-2013>, <http://www.atmos-chem-phys.net/13/2445/2013/>, 2013.

Sharan, M., Yadav, A. K., Singh, M., Agarwal, P., and Nigam, S.: A mathematical model for the dispersion of air pollutants in low wind
5 conditions, *Atmospheric Environment*, 30, 1209–1220, 1996.

Varon, D. J., Jacob, D. J., McKeever, J., Jervis, D., Durak, B. O. A., Xia, Y., and Huang, Y.: Quantifying methane point sources from fine-scale satellite observations of atmospheric methane plumes, *Atmospheric Measurement Techniques*, 11, 5673–5686, <https://doi.org/10.5194/amt-11-5673-2018>, <https://www.atmos-meas-tech.net/11/5673/2018/>, 2018.

Veefkind, J., Aben, I., McMullan, K., Förster, H., De Vries, J., Otter, G., Claas, J., Eskes, H., De Haan, J., Kleipool, Q., et al.: TROPOMI
10 on the ESA Sentinel-5 Precursor: A GMES mission for global observations of the atmospheric composition for climate, air quality and ozone layer applications, *Remote Sensing of Environment*, 120, 70–83, 2012.

Velazco, V. A., Buchwitz, M., Bovensmann, H., Reuter, M., Schneising, O., Heymann, J., Krings, T., Gerilowski, K., and Burrows, J. P.: Towards space based verification of CO₂ emissions from strong localized sources: fossil fuel power plant emissions as seen by a CarbonSat constellation, *Atmospheric Measurement Techniques*, 4, 2809–2822, <https://doi.org/10.5194/amt-4-2809-2011>, <https://www.atmos-meas-tech.net/4/2809/2011/>, 2011.

15